RESEARCH ARTICLE

Key Points:
- Venus air temperatures above clouds are driven by atmosphere dynamics
- Cloud altitude increases toward the equator also on the nightside
- [CO] at 65-70 km increases from 40S to 60S

Correspondence to:
D. Grassi,
davide.grassi@iaps.inaf.it

The Venus nighttime atmosphere as observed by the VIRTIS-M instrument. Average fields from the complete infrared data set

D. Grassi[1], R. Politi[1], N. I. Ignatiev[2], C. Plainaki[1], S. Lebonnois[3], P. Wolkenberg[4], L. Montabone[3,5], A. Migliorini[1], G. Piccioni[1], and P. Drossart[6]

[1]Institute of Space Astrophysics and Planetology, National Institute of Astrophysics (IAPS-INAF), Rome, Italy, [2]Space Research Institute of the Russian Academy of Sciences (IKI-RAS), Moscow, Russian Federation, [3]Laboratory of Dynamical Meteorology, National Council for Scientific Research (LMD-CNRS), Paris, France, [4]Space Research Center of the Polish Academy of Sciences (CBK-PAS), Warsaw, Poland, [5]Space Science Institute (SSI), Boulder, Colorado, USA, [6]Laboratory of Space Studies and Astrophysical Instrumentation of the Paris Observatory (LESIA-OBSPM), Meudon, France

Abstract We present and discuss here the average fields of the Venus atmosphere derived from the nighttime observations in the 1960–2350 cm^{-1} spectral range by the VIRTIS-M instrument on board the Venus Express satellite. These fields include: (a) the air temperatures in the 1–100 mbar pressure range (~85–65 km above the surface), (b) the altitude of the clouds top, and (c) the average CO mixing ratio. A new retrieval code based on the Bayesian formalism has been developed and validated on simulated observations, to statistically assess the retrieval capabilities of the scheme once applied to the VIRTIS data. The same code has then been used to process the entire VIRTIS-M data set. Resulting individual retrievals have been binned on the basis of local time and latitude, to create average fields. Air temperature fields confirm the general trends previously reported in Grassi et al. (2010), using a simplified retrieval scheme and a more limited data set. At the lowest altitudes probed by VIRTIS (~65 km), air temperatures are strongly asymmetric around midnight, with a pronounced minima at 3LT, 70°S. Moving to higher levels, the air temperatures first become more uniform in local time (~75 km), then display a colder region on the evening side at the upper boundary of VIRTIS sensitivity range (~80 km). As already shown by Ignatiev et al. (2008) for the dayside, the cloud effective altitude increases monotonically from the south pole to the equator. However, the variations observed in night data are consistent with an overall variation of just 1 km, much smaller than the 4 km reported for the dayside. The cloud altitudes appear slightly higher on the evening side. Both observations are consistent with a less vigorous meridional circulation on the nightside of the planet. Carbon monoxide is not strongly constrained by the VIRTIS-M data. However, average fields present a clear maximum of 80 ppm around 60°S, well above the retrieval uncertainty. Once the intrinsic low sensitivity of VIRTIS data in the region of cold collar is kept in mind, this datum is consistent with a [CO] enrichment toward the poles driven by meridional circulation.

1. Introduction

Venus has regained interest in the large planetary community after the successful orbit insertion of ESA's Venus Express satellite (VEX) on April 2006. The VEX payload has demonstrated to be particularly suitable for the atmospheric investigations, producing a data set of several years that allows now to characterize the Venus conditions on statistical basis. These studies have acquired a particularly significance since it has become clear that Venus: (a) may provide deep insights on the onset of runaway greenhouse effect [e.g.: *Ingersoll*, 1969; *Driscoll and Bercovici*, 2013], and (b) represents an important analogue for the study of Earth-size exoplanets located on the (yet poorly defined) inner edge of the habitable zone [*Abe et al.*, 2011].

In this context, an extensive characterization of the average state of the Venus atmosphere becomes particularly desirable as a starting point for more advanced studies. We have already discussed in *Grassi et al.* [2010] (paper I hereafter), the specific characteristics of the VIRTIS-M and provided a preliminary description of the average air temperature fields derived from its data. The present work aims to complete that discussion following two rationales: (a) the use of a more advanced algorithm, able to retrieve simultaneously the effective cloud top altitude and the average CO mixing ratio [CO], and (b) the processing of the entire data set acquired by VIRTIS-M during the operative lifetime of the IR cryocooler. At the current date, our approximate forward

radiative transfer algorithms are not yet capable to reproduce properly the CO features observed in Venus spectra at the resolution of VIRTIS-H. Consequently, the analysis of the data set returned by this subsystem had to be postponed to a future work.

2. The VIRTIS-M Data

While the main characteristics of VIRTIS instruments are given in paper I and in *Piccioni et al.* [2007], we briefly remind here the facts more relevant for the discussion.

VIRTIS-M is (along with VIRTIS-H) a subsystem of the VIRTIS (Visual and Infrared Thermal Imaging Spectrometer) instrument. VIRTIS-M is a spectro-imager, able to acquire simultaneously the spectra of 256 spatially contiguous, aligned pixels (a "slit"). Each spectrum covers the range 0.4–5.1 μm (25,000–1960 cm^{-1}), with a spectral sampling of 1.9 nm (between 0.4 and 1 μm, i.e., 25,000–10,000 cm^{-1}) or 11 nm (in the 1.–5.1 μm range, i.e., 10,000–1960 cm^{-1}).

Repetition of the slit acquisition with different pointings (achieved either by the instrument internal scanner or by the spacecraft motion) allows one to build a "cube," i.e., a bi-dimensional image where we have a full spectrum for each pixel. The field of view for an individual pixel of VIRTIS-M (IFOV) is 0.25 × 0.25 mrad. This value corresponds to a horizontal resolution for individual pixels of 16.5 × 16.5 km in the case of measurements acquired at the VEX apocenter.

On-ground and on-board calibrations provided an estimate of the noise equivalent radiance in conditions of zero signal (i.e., without photon noise contribution from the observed scene) equal to $8 \cdot 10^{-3}$ $\mu W/(m^2 \, ster \, m^{-1})$ at 2000 cm^{-1}.

In this work we considered the values of VIRTIS spectral sampling points centers and effective resolution as given in the VIRTIS-M calibration document (available at ftp://psa.esac.esa.int/pub/mirror/VENUS-EXPRESS/ VIRTIS/) for the central part of the slit and the effective temperature of the instrument of 155 K. The instrument is known to vary slightly these parameters depending on slit position and instrument thermal conditions, but a satisfactory empirical modeling of these effects is not yet available. We preferred therefore to avoid the introduction of further corrections that could easily result in additional sources of error.

Most of the cubes used in this work were acquired at the VEX apocenter (located above the Venus south pole), scanning the disk with the VIRTIS internal pointing mirror. In these cases, the spatial resolution is worse, but the slower orbital motion allowed the instrument to acquire wide global mosaics of the southern hemisphere. A small percentage of cubes (5%) were taken scanning the planet using the orbital motion of the spacecraft. These data cover a larger span of latitudes at higher spatial resolution but in very narrow stripes along meridians.

Air temperature retrieval can be performed inverting the observed atmospheric thermal emission, exploiting the variable opacity of CO_2 inside its 4.3 μm (2325 cm^{-1}) band [*Grassi et al.*, 2008]. In daytime, radiance in this spectral region is dominated by the reflected sunlight and, in the most opaque parts, by the CO_2 non-LTE emission [*Gilli et al.*, 2009]. At the current state of our modeling tools, it is not possible to disentangle these contributions with an acceptable speed; therefore, in this work we had to limit the study to the nighttime data. In order to avoid the signal saturation by the instrument thermal emission in the region above 3.5 μm (2860 cm^{-1}), we had to consider only the data acquired with exposure times below 0.36 s and active cryocooler.

These constraints reduce the suitable VIRTIS-M data set to 636 cubes, acquired between orbits 23 and 847 (14 May 2006 to 15 August 2008). This data set needed to be preprocessed before the analysis by the actual retrieval code. This phase included a statistical study of the cube values, mostly aimed to detect and mask cube regions affected by the impinging of cosmic rays. The masked cubes were then averaged, in the spatial dimension, in bins of 4 × 4 pixels (ignoring masked data). This procedure obviously reduced the spatial resolution but allowed: (a) to achieve acceptable processing times and (b) to remove the high-frequency spatial variations of the signal observed along the slit (the so-called "odd-even effect"), which were occasionally left behind by calibration procedures.

3. Retrieval Code Concepts

A full retrieval scheme for VIRTIS data based on the Bayesian formalism [*Rodgers*, 2000] was first presented by *Irwin et al.* [2008a] (paper II hereafter) as a specific optimization of their well-established NEMESIS code
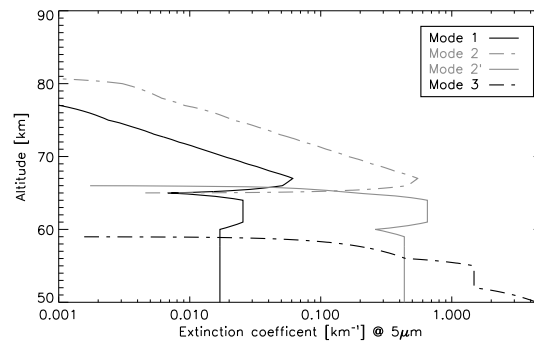
Figure 1. Reference extinction coefficients for the different aerosol modes included in the radiative transfer computations. Plots refer to the wavelength of 5 μm (2000 cm^{-1}). The retrieval code varies the cloud top altitude applying a scalar (i.e., constant along altitude) multiplicative factor to these profiles. The multiplicative factor has the same (variable) value for modes 2, 2′, and 3, while it is kept fixed to one for mode 1.

[*Irwin et al.*, 2008b]. More recently, *Kappel et al.* [2012] and *Haus et al.* [2013], developed another Bayesian code, inclusive of the retrieval of cloud effective altitude.

Our own new implementation, presented here, aims mostly to merge the benefits of the fast subroutines for the forward radiative transfer (already adopted in the code described in *Grassi et al.* [2008], based on a relaxation approach) with the formal robustness of the Bayesian approach, to obtain a tool able to process the entire VIRTIS data set in a reasonable time.

3.1. Atmosphere Model

Our new code models the atmosphere of Venus as a stack of 67 fixed pressure levels, uniformly spaced along the logarithm of air pressure, between 1200 and $5 \cdot 10^{-3}$ mbar (~ 50.–106. km). The retrieval scheme considers the air temperatures at these levels as the main unknown parameters to be retrieved.

The code assumes the number and properties of aerosol modes described in *Zasova et al.* [2007], ultimately derived from *Knollenberg and Hunten* [1980]. Namely, size distributions (modes 1, 2, 2′, and 3), composition (75% H_2SO_4, 25% H_2O), and *relative* aerosol density vs. altitude (for each of the four modes) are kept fixed during the retrieval. The retrieval code is allowed to vary the effective altitude of the clouds by changing the value of just *one* scalar multiplicative factor, to be applied to the reference profiles of aerosol densities vs. altitude. Extinction coefficients corresponding to these profiles are presented in Figure 1. The *same* factor is applied to all altitude levels for aerosol modes 2, 2′, and 3. Densities of mode 1 particles are not varied. Once the *current* aerosol density profiles are determined by the multiplication, we can define the effective cloud top altitude as the level of $\tau = 1$ at the reference wavelength of 1.21 μm (8264 cm^{-1}), which allows us to compare with the results of *Ignatiev et al.* [2009].

CO_2 and CO are assumed to have a constant mixing ratio with altitude. The [CO_2] is assumed equal to 0.965 while [CO] is retrieved by the code for each spectrum, on the basis of the shape of its main band located at 4.6 μm (2174 cm^{-1}). Paper II provides an extensive discussion of sensitivity of VIRTIS-M data to CO content.

The state vector to be retrieved (*x*, in the Rodger's formalism) consists therefore in an array of 69 scalar elements. Instead of retrieving the absolute multiplicative factors for aerosols and CO, we preferred to consider as unknown their respective logarithms. This choice forces the multiplicative factors to be always strictly positive and avoids unrealistic negative values. While this approach may not be suitable when dealing with quantities virtually equal to zero (e.g., determination of detection thresholds for minor species), it is fully justified in this context, since CO and aerosol are known to be always present.

3.2. Approximations of the Forward Radiative Transfer Model

To achieve a reasonable computational time, approximations need to be adopted to model the forward radiative transfer processes and to derive the spectrum *F(x)* expected for a given *x*. Eventually, we need to compare this quantity to our actual VIRTIS-M spectrum (*y*, in the Rodger's formalism).

CO_2 transmissions are evaluated by the pre-convoluted transmission method, originally developed for the modeling of the Venus CO_2 15 μm (667 cm^{-1}) band [*Schaefer et al.*, 1987] and successfully adopted for Mars [e.g.: *Grassi et al.*, 2005] and Venus [*Grassi et al.*, 2008]. The pre-convoluted transmittances are computed considering the opacity of CO_2 in the 4.3 μm region (around 2325 cm^{-1}) expected by the model of *Tran et al.* [2011], inclusive of the line-mixing effects. The pre-convoluted transmittances are not yet providing satisfactory accuracy in the CO_2 transparency windows, where thermal radiation may escape from the lower atmosphere (2.3 and 1.71 μm, 4350 and 5850 cm^{-1}). Consequently, we were forced to disregard these spectral regions in our analysis, despite their valuable information content for vertical aerosol distribution [*Haus et al.*, 2013].

CO transmittances for variable mixing ratios are derived according to the Curtis-Godson approach. In the computation of CO tables, we considered the CO line parameters listed in the HITRAN 2008 database [*Rothman et al.*, 2009]. The Voigt line shape was assumed, truncating line wings $35\,cm^{-1}$ away from respective centers.

Multiple scattering is taken into account solving the radiative transfer problem by mean of the "layer flux adding procedure" [*Isaacs et al.*, 1987]. Particles are assumed to be spherical and a Mie code is used to derive the Legendre expansion of their phase functions up to the 48th term.

3.3. Assumed a Priori and Its Covariance Matrix

A priori state vector (x_a) and its covariance matrix (S_a) may have a key influence in final results of highly underconstrained retrievals, which is a common condition in remote sensing problems, also occurring here.

For air temperatures, at each pressure level in our vertical grid, we assumed as a priori the mean of values retrieved from Venera 15 FTS data [*Zasova et al.*, 2007]. For the aerosol multiplicative factor, a priori was set equal to one (zero in the logarithmic space) while for [CO] we considered as a priori the mean value of 40 ppm quoted by paper II.

For the overall structure of S_a matrix, we set to zero every off-diagonal element related to aerosol and CO. This means that we did not impose in our solutions any statistical correlation between aerosol densities and air temperatures or between [CO] and air temperatures. Conversely, air temperatures at adjacent levels cannot be considered as statistically independent and we assumed a correlation in the form of

$$C_{i,j} = \exp\left(-(z_i - z_j)^2/h_c^2\right).$$

Here, i and j are indexes to designate different pressure levels, z_i and z_j their respective altitudes (in the a priori temperature profile), and h_c is an effective correlation length.

Ideally, h_c and the variances σ_a^2 of the state vector elements (i.e., diagonal elements of S_a) shall be derived exclusively from the analysis of available climatology (a priori information), but several practical issues (e.g., ambiguities in defining the effective vertical resolution of Venera 15 retrievals, limited coverage, different reference wavelength for cloud altitude) precluded this straight approach. As a matter of fact, h_c and the σ_a^2 are free parameters of our retrieval scheme, to be tuned during the validation phase of the code. Tests on simulated observations and on a limited set of actual VIRTIS data demonstrated a non negligible dependence of final results on the adopted values. Nevertheless, they also pointed toward a rather defined set of values, suitable to minimize the retrieval error and to maximize the probability to achieve convergence. These values include: (a) an h_c comparable to the typical widths of weighting functions for air temperatures, and (b) values of σ_a slightly smaller than the corresponding actual standard deviations in the input state vector elements considered to generate simulated data set.

The results presented in this paper were achieved considering $h_c = 7.5\,km$, σ_a(air temperature) $= 4\,K$ (for all levels), $\sigma_a(\log_{10}$(aerosol multiplier)) $= 0.3$, and $\sigma_a(\log_{10}$(CO multiplier)) $= 0.3$.

3.4. Assumed Measurement Errors and Corresponding Covariance

In ideal conditions (i.e., no systematic calibration artifacts), measurement errors in different sampling points of the spectrum display zero statistical correlation, leading to a diagonal form for the S_e matrix. The simplest hypothesis for this quantity is therefore:

$$S_e(m, n) = NER_m \cdot NER_n \cdot \delta^m_n,$$

where m and n are indexes to define different spectral sampling points, and NER indicates the noise equivalent radiance of the instrument. We assumed for the NER the estimates from calibration measurements (see again the calibration document at ftp://psa.esac.esa.int/pub/mirror/VENUS-EXPRESS/VIRTIS/), for conditions of zero signal. This value was further divided by 4 to account for the average process of adjacent spatial pixels described in section 2.

This NER figure represents just a lower limit for actual measurement errors. A first obvious source of additional error is represented by the photon noise of the source. More interestingly, measurement errors provide a direct
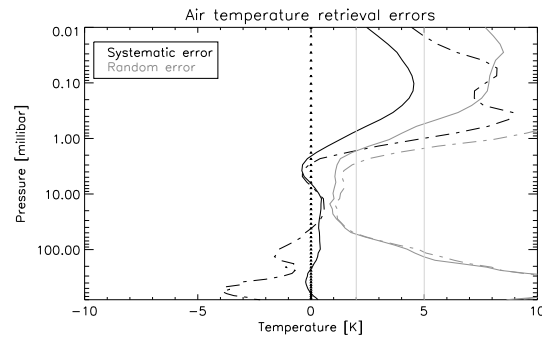
Figure 2. Retrieval errors on air temperatures, as estimated from numerical tests on *simulated* VIRTIS observations. Black: systematic error, Gray: random error. Solid: assuming the nominal NER value, dash-dotted: including the modeling residuals observed on real Venus data.

way to account for the approximations of forward models in the retrieval scheme. An extended discussion on this subject is given in section 5.1.

3.5. Code Implementation

In order to increase the degree of linearity of the problem, we considered as observable **y** not the radiances but the equivalent brightness temperatures. Even in this form, we found necessary to adopt the Levenberg-Marquardt method given in equation 5.36 of *Rodgers* [2000], to avoid the rapid growth of unrealistic temperature profiles.

For each spectrum, the code was allowed a maximum of 20 iterations to achieve the convergence. The convergence criterion was established by the comparison, at each iterative step, of the magnitude of the update in the state vector with its expected covariance matrix. Namely, considering eq. 5.29 of *Rodgers* [2000], we required that d_i^2/n becomes smaller than 0.005.

The Jacobian matrix (**K** in the Rodgers formalism) was computed by direct numerical differentiation at each iterative step, since inclusion of multiple scattering makes the explicit differentiation of the forward model a prohibitive task. Preliminary tests demonstrated that, even considering the CO_2 transmittance as expected by the modeled by *Tran et al.* [2011], our code was not able to model satisfactory short-wavelength side of 4.3 µm band (wavenumbers higher than $2350\,cm^{-1}$). For spectral-fit purposes, therefore, the code considered only the range between 4.25 and 5.1 µm ($2350–1960\,cm^{-1}$).

4. Validation Using Simulated Observations

Following the same approach adopted in *Grassi et al.* [2008], we extracted from the Venera 15 FTS retrievals a subset of 182 T(p) profiles, distributed as uniform as possible in the local time/latitude space. Despite this effort, the selected profiles refer mostly to high-latitude locations because of the observational bias imposed by the orbit of Venera 15 satellite. We also generated a series of 182 random values for the logarithm of the multiplicative value for CO mixing ratio and a series of 182 random values for the logarithm of multiplicative value for aerosol mixing ratios. More specifically, resulting [CO] values vary between 3 and 480 ppm, with a standard deviation of 70 ppm, while cloud top altitudes vary between 69 and 74 km, with a standard deviation of about 1 km. These data together allowed defining 182 different state vectors, which were used to compute the corresponding expected VIRTIS spectra (for zero degrees emission angle). The code used to compute synthetic spectra was the same embedded in the retrieval code. Eventually, we added to the simulated observations a random noise, whose statistical properties are given by the S_e matrix given in section 3.4 (noise is recomputed with a different set of random values for each spectrum). The resulting simulated VIRTIS spectra were provided as input to our retrieval code, to evaluate its performances on statistical basis.

4.1. Modeling Performance

The code was able to achieve a very good modeling performance on simulated data. The χ^2 statistic is strongly peaked around value 1 while—in the spectral range considered for the spectral fit—the statistics of residuals (observed—best fit spectra) show an average value very close to zero (i.e., no systematic error), and a random value basically identical to the noise imposed to data.

4.2. Retrieval Performance

A case-by-case comparison between the values of the input state vector and those retrieved by the code from simulated observations allowed a statistical assessment of retrieval capabilities.

Air temperatures were retrieved in the entire region 1–100 mbar (~ 85.8–65. km) with a systematic error smaller than 1 K (Figure 2). Random errors remained below 2 K between 1.2 and 50 mbar (~ 85–68.1 km) and below 5 K between 0.7 and 90 mbar (~ 87.2–65.2 km). Similarly, the altitude of the cloud top was retrieved with a negligible systematic error (0.04 km) and a random error of 0.65 km. As already pointed out by paper II,
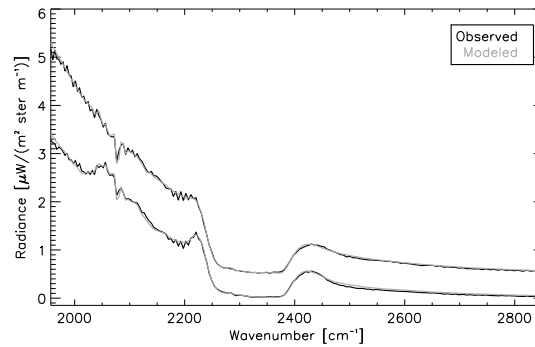
Figure 3. Examples of observed VIRTIS-M spectra and corresponding best fit spectra produced by the retrieval code. For clarity, upper spectrum has an offset along y axis of $1\,\mu W/(m^2\,ster\,m^{-1})$. Both examples are from cube VI00038_02.

retrieval of [CO] was subject to more substantial uncertainties: while the systematic component remained low ($-1.2\,ppm$), the random error reached a value of 13.1 ppm, i.e., about 30% of the typical CO concentrations reported by paper II. Noteworthy, a substantial fraction of the input temperature profiles referred to the conditions of the north cold collar, where, according to paper II, we may expect an increased retrieval error for [CO] because of the temperature inversions observed there. To confirm this interpretation, we repeated the test adopting a constant T(p) profile with a strong thermal gradient around 65 km. In this run, random retrieval error on [CO] was reduced to 5.2 ppm.

Retrieval errors derived from this test shall, however, be considered as optimistic limits of the actual performance on real VIRTIS data. Simplified aerosol properties and approximations of adopted forward radiative transfer models are two likely sources of additional errors. In this view, section 5.1 describes an approach to estimate more realistic retrieval errors.

5. Results on Actual VIRTIS-M Data

The code described in section 3 was applied to the entire set of VIRTIS-M data acquired during the operative lifetime of the cryocooler, resulting in a set of more than $2\cdot10^6$ individual retrieved state vectors.

This data set enables several opportunities of analysis. In this work, we limit our focus on the average properties of the Venus atmosphere, to validate and to extend the results we previously reported in paper I.

5.1. Overall Modeling Performance and Updated Retrieval Performance Estimates

Once the code was applied to the real data, it was not able to achieve the excellent modeling performance obtained on simulated observations (Figures 3 and 4). Even considering only the cases where the convergence criterion described in section 3.5 was satisfied, the differences between observed and best fit spectra show a systematic component well above the assumed NER in several spectral regions within the range adopted for modeling. The random component of the residuals has usually a value about four times larger than the assumed NER level. Correspondingly, χ^2 statistics is strongly peaked around a value of about 25.

These residuals can have several different origins. We focused our attention on the approximations in the modeling of gaseous transmittance. For this purposes, we compared the 182 simulated observations described in section 4 (before adding noise) with the corresponding spectra computed by a line-by-line approach (Figure 5). Both systematic and random components of these differences are well below the values observed in Figure 4. Therefore, approximations in gaseous transmittance treatment can justify only a part of the observed residuals.

Other sources of discrepancies—more difficult to quantify—can potentially be represented by the following:

1. The approximate model of aerosols (size and optical properties), too simplified or inadequate with respect to the actual Venus conditions. The assumption of constant properties in space and time is particularly strong.
2. Approximations in the treatment of multiple scattering by the layer flux adding procedure.
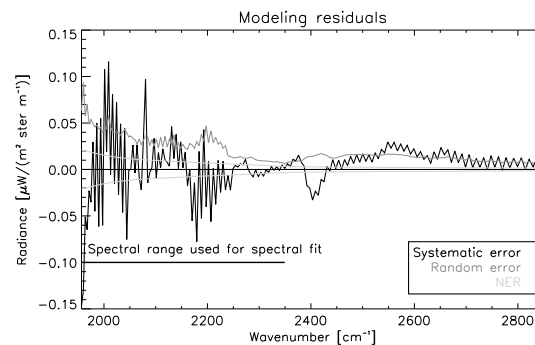

Figure 4. Statistic on the differences between observed and best-fit spectra, as derived from the analysis of the entire VIRTIS data set.
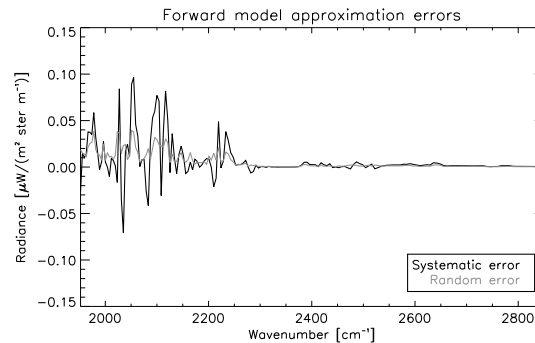
Figure 5. Comparison between synthetic spectra computed by the approximate subroutine used in the retrieval code and line-by-line counterparts.

3. The assumption of *relative* constant profiles of aerosols with respect to altitude. Just one free parameter (scalar multiplier) may be insufficient to describe the role of cloud variations in VIRTIS spectra.

4. The assumption of uniform [CO] along the altitude. Paper II demonstrated that VIRTIS data are mostly sensitive to altitudes around 68 km, and therefore this approximation shall not have a major impact on our modeling capabilities.

5. Residual errors in the adopted values for VIRTIS spectral resolution and sampling grid. This hypothesis is qualitatively consistent with the high-frequency components of the systematic differences. Fu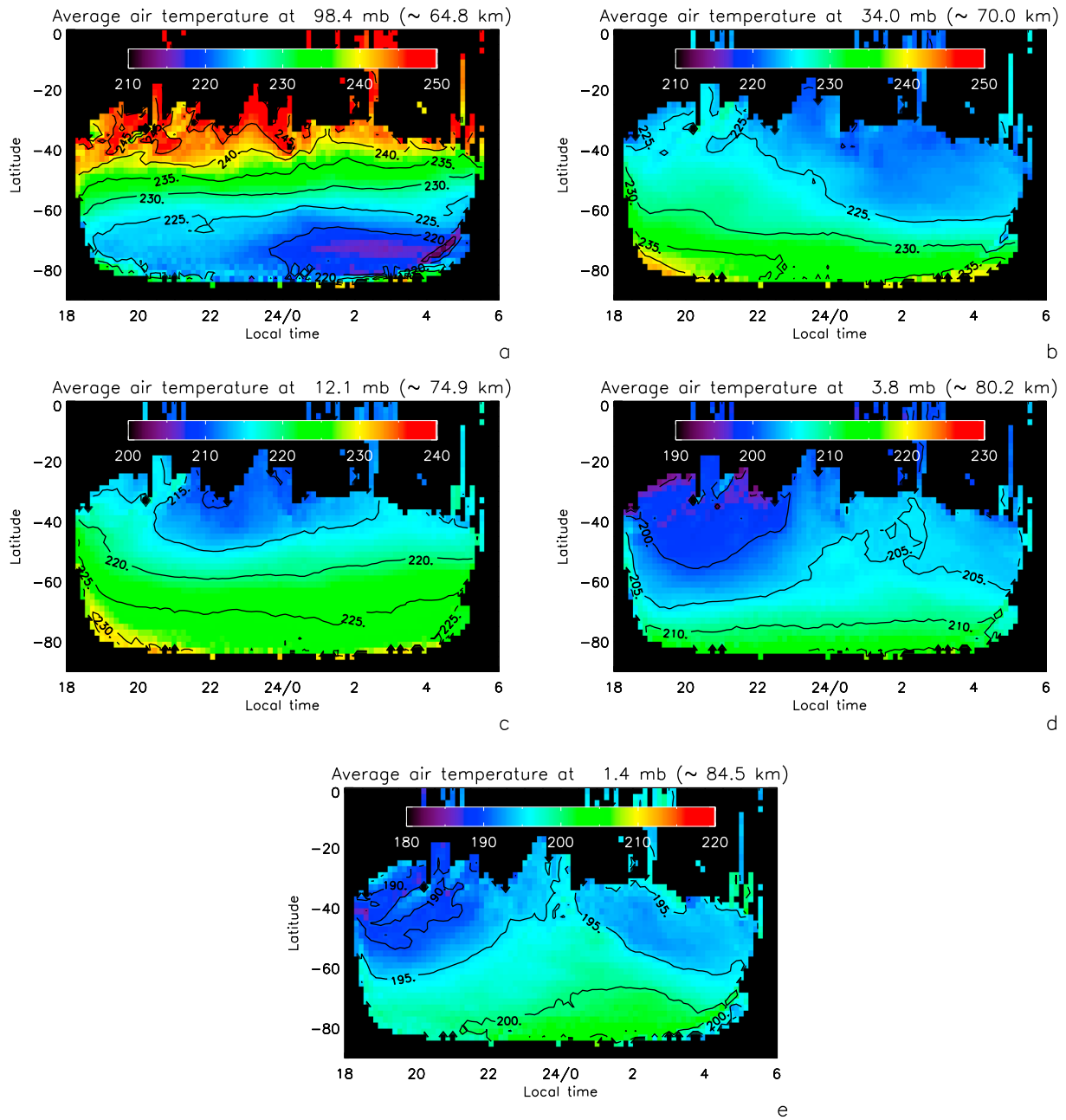rthermore, the variations of these parameters along the slit or with spectrometer temperatures can represent another source of residuals when the entire data set is considered. Minor calibration artifacts may contribute both to systematic and random components of residuals. Adopted NER values may also be underestimated with respect to the actual values.

Regardless the actual source of spectral residuals, their effects on retrieval results can be quantified by repeating the validation tests on simulated spectra, as described in section 4, with the addition of: (a) adding to each simulated spectrum the systematic residual given in Figure 4, and (b) adding a random noise with the same statistic of random residual given in Figure 4. This approach—adopted also in *Tice et al.* [2013]—provided us with updated information on retrieval performance.

Air temperature retrieval errors are presented as dashed lines in Figure 2. The region where the random error is below 2 K is now reduced to the range 3–50 mbar (~ 81.2–68.1 km). The random error lies below 5 K between 1.2 and 90 mbar (~ 85.0–65.2 km). Noteworthy—for both reference values of error—the confidence region is substantially reduced only in the upper levels, where information is derived from the inner parts of the CO_2 band, more prone to additional noise because of their overall lower signal level. Higher parts of the sensitivity range (above the 2 mbar level, ~ 82.9 km) are also relatively more affected by the rapid growth of systematic retrieval errors. Their magnitude remains, however, below 1.5 K between 1 and 100 mbar (~ 85.8–65.0 km).

The performance on the retrieval of aerosol cloud top is not subject to substantial degradation in the updated estimate. The systematic component of the retrieval error remains very low (−0.13 km) as well as the random contribution (0.67 km). Conversely, the performance on [CO] retrievals is more strongly affected: while the systematic component remains relatively low (2.85 ppm), the random error increases up to 18.1 ppm. Even in this new evaluation, however, true and retrieved values of [CO] mixing ratio retain a correlation coefficient equal to 0.95.

5.2. Retrievals Post-Processing

The retrieved population of state vectors derived from real VIRTIS data was filtered to accept only the cases where:

1. we have an 'acceptable' match between observations and best fit simulated spectra (quantified by a $\chi^2 < 50$. if computed by considering the original NER; this value corresponds to a χ^2 of about 3 if one considers the random modeling error of Figure 4);

2. the emission angle is smaller than 30° (to limit uncertainties related to approximate forward modeling of the radiative transfer);

3. the solar incidence angle is greater than 95°, to remove cases with residual non-LTE emission at the bottom of the 4.3 μm (2325 cm^{-1}) band.

The elements of the resulting selected population (about $9.3 \cdot 10^5$ individual state vectors) were binned according to local time and latitude. We chose a bin size value of 2° for both latitude and local time. Inside each cell of this local time/latitude grid, we can now define a set of different estimates (one estimate = one individual retrieval) for each element of the state vector (67 air temperatures at the different levels of the pressure grid, cloud top altitude, [CO]). Each set is filtered to remove outliers that lie more than 2σ away from the mean value. Selected elements are eventually averaged to create the mean fields presented in Figures 6, 8, and 9.

Figure 6. Average air temperature field of the Venus atmosphere at different pressure levels, as retrieved from VIRTIS-M data.

5.3. Average Temperature Fields

The average temperature fields at five different pressure levels are presented in Figure 6. These can be compared with the previous results of Figure 3 in paper I.

The level of 98 mbar (~64.8 km, panel a) lies at the lowest boundary of our sensitivity range. Here, the cloud effective opacities often exceed the unit value, and temperature retrieval errors are strongly correlated to absolute cloud opacity and to retrieval errors on the altitude of the cloud top. Taking these effects in due consideration, we can confirm one of the main findings of paper I: at 75°S we can observe a strong cooling of the atmosphere at 3LT with respect to evening local times. The monotonic longitudinal increases of air temperature from the region of the cold collar toward the equator and toward the south pole are also confirmed. With respect to results of paper I, we can observe: (a) a shift toward higher latitudes of the region
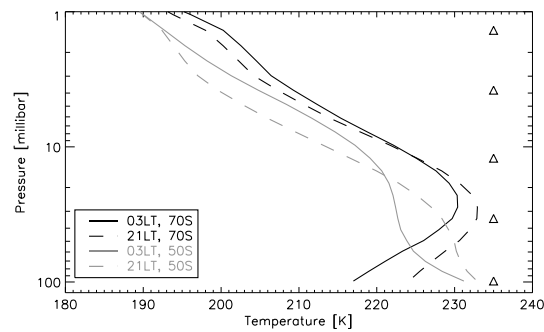
Figure 7. Average T(p) profiles at selected local times and latitudes. Triangles mark the pressure levels displayed in Figure 6.

of minimum temperature, (b) a general increase of temperature values (>5 K) and of latitudinal temperature gradients for the regions northward of 50°S, and (c) reduced latitudinal temperature gradients southward of 70°S. While it is difficult to quantitatively explain these differences between the two approaches, our preferred hypothesis consists in the different treatment of aerosol altitudes between the algorithm presented here and the one adopted in paper I. The latter basically assumed a fixed altitude, equal to about 71.7 km. The cloud top altitudes presented below (see section 5.4) show a weak but clear increase from the pole toward the equator. Consequently, at this pressure level we observe a larger opacity toward the equator, and a smaller opacity toward the pole with respect to the assumption in paper I. At a fixed radiance value and air temperatures decreasing with altitude, this induces higher retrieved temperatures toward the equator and lower retrieved temperatures toward the poles, as actually observed here. Noteworthy, despite retrieval uncertainties related to aerosols, our results at this pressure level are in excellent quantitative agreement with the retrievals from VeRA data (Tellmann et al., in preparation, 2013), that are not prone to adverse effects of clouds. VIRTIS retrievals are also in agreement with the results of *Encrenaz et al.* [2013], who—on the basis of ground-based observations of the continuum thermal emission of the cloud top at 7 μm (1428 cm^{-1})—estimated an air temperature difference of about 10 K between the evening and the morning terminator around this pressure level at 70°S.

The level at 34 mbar pressure (~70.0 km, panel b) shows a strong evening-morning asymmetry, particularly marked north of 60°S, where the morning side can be colder about 5 K. Above this level, air temperatures are monotonically decreasing from the pole toward the equator for all local times. For this altitude, the cloud opacity is already much smaller than 1 at all longitudes, and therefore it is not surprising that we essentially confirmed the results of paper I.

At 12.1 mbar (~ 74.9 km, panel c) the air temperature fields are remarkably symmetric with respect to midnight. The only relevant feature remains the cold region at 40°S, 23LT, which does not have a morning counterpart. Again, we observe a very good agreement with results from paper I: the slight increase of temperatures around midnight south of 70°S described there is, however, completely smeared out in the new data set.

The pressure level of 3.8 mbar (~80.2 km, panel d) shows, north of 70°S, a morning side warmer than its evening counterpart (5–10 K at 40°S), as already described in paper I. This finding is consistent with the cooling on the evening side around 40°S that VeRA observes when moving between 4 mb and 1 mb (~85.8 km) levels (Tellmann et al., in preparation, 2013)

The validation procedure described in section 5.1 justifies a cautious inspection of the average field at 1.4 mbar pressure level (~84.5 km, panel e). Even if temperatures remain slightly higher on the morning side, average fields become more symmetric around midnight, where a local maximum appears north of 50°S.

The sensitivity range of VIRTIS spans over about 20 km in altitude, where air temperatures exhibit complex relations with local time. This fact suggests a key role of dynamic in shaping Venus nighttime air temperature fields. Particularly interesting is the overall temperature variation with local time at different altitudes, better seen in the selected complete T(p) profiles presented in Figure 7. While morning side is colder at 34 mbar (~70.0 km), it shows similar values to evening counterpart at 12.1 mbar (~ 74.9 km), becomes warmer at 3.8 mbar (~80.2 km) and seems to reduce again the difference at 1.4 mbar (~84.5 km). *Migliorini et al.* [2012], used the LMD Venus global circulation model [*Lebonnois et al.,* 2010, 2012] to interpret the VIRTIS-H observations in term of thermal tides. They concluded that the signal of the semi-diurnal tide was present at equatorial and low latitudes, while the signal at high latitudes was likely to be interpreted as the diurnal component of the tides. In the VIRTIS-M observations discussed in the present paper, we clearly observe the shift of the phase of the semi-diurnal component with altitude, as shown in Figure 5 of *Migliorini et al.* [2012], for the GCM model (Note that the pressure levels do not necessarily correspond between model and observations). This strong similarity between observations and model results will require further work to
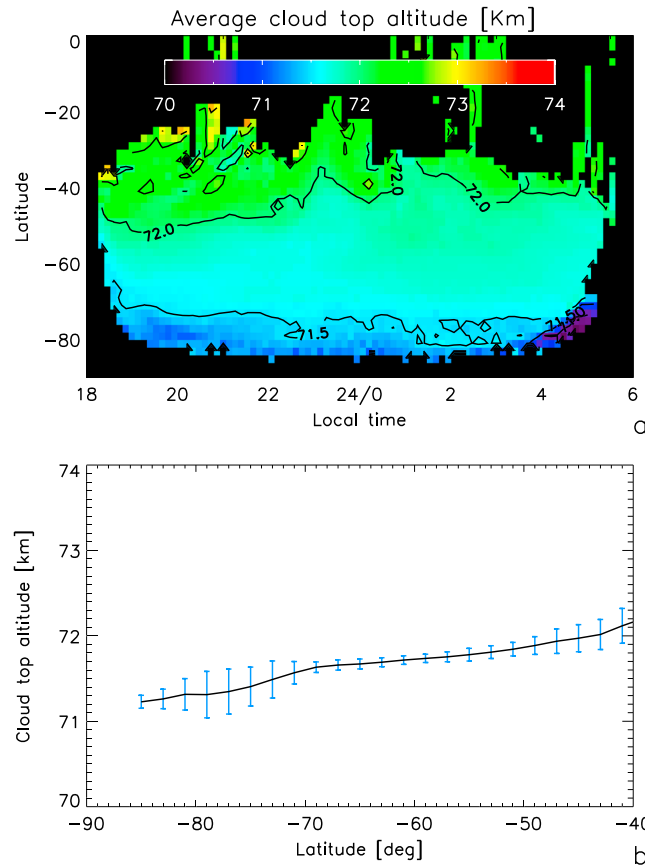
Figure 8. Average altitude of the cloud top, as retrieved from VIRTIS-M nighttime data. (a) As a function of local time and latitude. (b) As a function of latitude only, obtained averaging different local times. Vertical bars in each sampling point (center of averaging bin) show standard deviation inside each latitude strip.

establish the theoretical basis for the vertical propagation of the Venusian semi-diurnal component within the classical theory for migrating (i.e., Sun-synchronous) solar tides.

5.4. Average Cloud Top Altitude and [CO] Fields

Figures 8 and 9 show the average values of cloud top altitude and [CO] retrieved from VIRTIS data.

Our retrievals from VIRTIS nighttime data indicate a monotonous increase of the cloud top from the pole toward the equator (Figure 8). While the cloud top altitude does not display any peculiar local time trend south of 70°S, for lower latitudes we can observe higher altitudes on the evening side, where—consequently—latitudinal variations appear slightly more evident.

A rise of cloud top altitude toward the equator was first reported by *Kawabata et al.* [1980] and more recently confirmed on the basis of VIRTIS daytime data [*Ignatiev et al.*, 2009] and by SOIR data at both terminators [*Wilquet et al.*, 2012]. Both works also suggest higher clouds on the evening side. Despite this qualitative agreement, our latitudinal variations are considerably smaller than the values reported by other
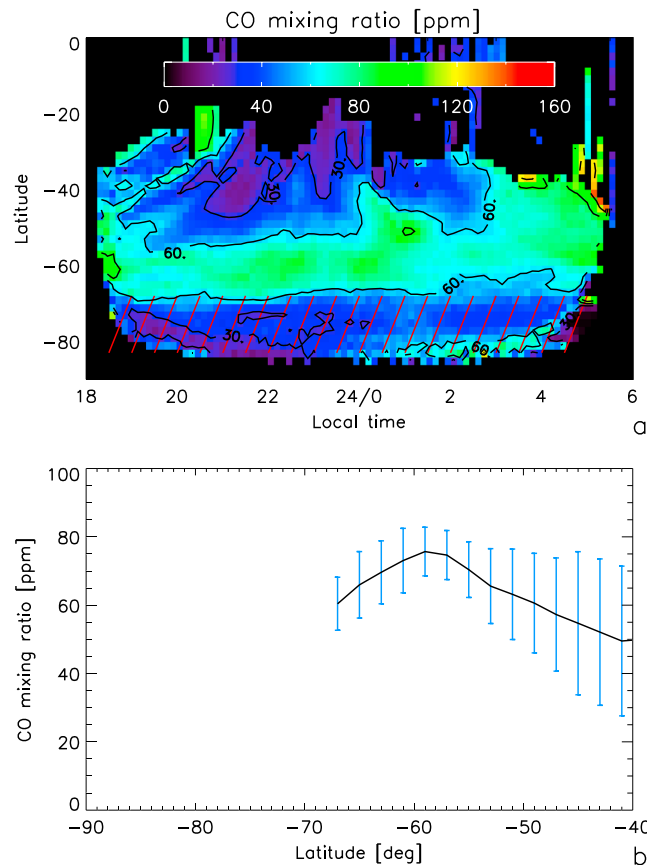
authors. Namely, our retrievals indicate a total rise of cloud top of just 1 km between 80°S and 40°S, while *Ignatiev et al.* observed in the same region a variation of about 4 km. We found particularly challenging to justify our small variations.

1. During tests on simulated observations, the retrieval code was able to properly retrieve cloud top altitudes in the entire range between 68 and 76 km. It is therefore unlikely that the adopted value of S_a element related to cloud profiles multiplier represented an excessive constraint on the solution.
2. A potential inconsistency is the different approach adopted to vary cloud top altitude (profile multiplier vs. vertical translation of cloud top at fixed absolute densities). In our preliminary tests we found that VIRTIS nighttime data in the spectral range considered for retrieval are not able to discriminate between the effects of these two approaches, and therefore we consider this assumption as marginal in producing the observed differences.
3. Both data sets define the altitude as the level of unity opacity at 1.21 μm (8264 cm^{-1}), but while in *Ignatiev et al.* [2009], this is the actual spectral range used for the retrieval, in our work the value shall be computed assuming a given ratio of aerosol opacities between our work region (5–4.25 μm, 2350–1960 cm^{-1}) and 1.21 μm. This assumption is ultimately derived from the adopted aerosol size distribution and composition.
4. *Ignatiev et al.* [2009] assumed a cloud only composed of mode 2 particles. Our preliminary tests demonstrated that the removal of other cloud components determines a worsening of spectral fit between 5 and 4.25 μm (2000–2350 cm^{-1}) that cannot be compensated by varying the quantities to be retrieved in the state vector. This observation implies that nighttime VIRTIS data cannot be processed in a consistent manner according to the assumptions of *Ignatiev et al.*, and it is therefore impossible for us to carry out numerical tests to assess the role of these assumptions in producing the observed differences.

Figure 9. Average CO mixing ratio, as retrieved from VIRTIS-M nighttime data. (a) As a function of local time and latitude. The pattern of diagonal lines south of 70°S is introduced to mark the region of typical occurrence of thermal inversion in the mesosphere, close to the 30 mbar level (~72 km). *Irwin et al.* [2008b] demonstrated that in these conditions the information content of VIRTIS data about CO is particularly low. Consequently, CO values retrieved here shall be disregarded. (b) As a function of latitude only, obtained averaging different local times. Vertical bars in each sampling point (center of averaging bin) show standard deviation inside each latitude strip.

Inspection of [CO] map (Figure 9) requires special caution due to the large retrieval error on individual measurements (about 20 ppm). Further limits of VIRTIS data in determining the [CO] are extensively discussed in paper II. Namely, these authors detailed the substantial uncertainties in retrievals in the area of the cold collar (around 70°S), where the temperature inversion usually observed between 65 and 70 km causes a strong decrease of the amplitude of CO spectral features and—consequently—in the data information content. Even with these facts in mind, VIRTIS retrievals point toward a clear local maximum of [CO] in the region around 60°S, where it reaches a peak of about 80 ppm. The region appears slightly more extended in latitude on the morning side. By comparison, the two orbits discussed by paper II show an increase of [CO] only north of 55°S and more pronounced on the *evening* side. That work reports for latitudes north of 50°S a value of [CO] between 40 and 60 ppm, and no obvious decrease north of 45°S. Interestingly, the [CO] latitudinal trends of our map seem to follow closely those reported by *Tsang et al.* [2008], for the [CO] at 35 km altitude, observed in the atmospheric windows of 2.35 μm (4255 cm^{-1}) in the same VIRTIS-M nighttime data used in this work. An increase of [CO] below the main cloud deck from the equator toward the poles (at least up to 60°S/N) was first reported by *Marcq et al.* [2005] and *Marcq et al.* [2006] from ground-based observations and further confirmed from VIRTIS-H data in *Marcq et al.* [2008].

6. Discussion

Our results on air temperatures are in excellent agreement with the values retrieved by *Migliorini et al.* [2012], on the basis of VIRTIS-H data for a larger latitudinal coverage. Following the approach adopted in that paper, we can attempt an interpretation of the observed fields in view of the results obtained by global circulation models (GCM) of the Venus atmosphere. Namely, we considered the simulations resulting from the LMD GCM described in *Lebonnois et al.* [2010], *Lebonnois et al.* [2012], and *Migliorini et al.* [2012].

Figure 5 in *Migliorini et al.* [2012] presents GCM simulations of the effects of thermal tides in average temperature fields, computed starting from a condition where superrotation is already established. An inspection of these results demonstrates that:

1. GCM predicts a semi-diurnal tide dominating at mid-latitudes and a diurnal tide dominating at high latitudes. Despite quantitative differences between model and observations, this overall structure is consistent with VIRTIS-M fields.

2. At high latitudes, the GCM does not model the cold collar, and the minimum of the diurnal tide is closer to 6.00LT than to 3.00LT. However, in the warm polar region at higher altitude, the gradient between the minimum and maximum values is more consistent with observations.

3. In VIRTIS-M fields the phase of the tides shifts toward earlier hours as one goes higher in altitude. This feature is reproduced by GCM simulations.

The polar warming observed in VIRTIS-M fields is consistent with the air subsidence related to the meridional circulation expected by the GCM [*Lebonnois et al.*, 2010]. Noteworthy, the GCM simulations strongly suggest that subsidence is going deeper in the cloud on the dayside than on the nightside. This may be consistent with stronger latitudinal contrast in the cloud top on the dayside compared to nightside, suggesting therefore that—at least partially—the difference of our results of Figure 8 (VIRTIS-M night data) and those of *Ignatiev et al.* (VIRTIS-M day data) may reflect a real condition of Venus' atmosphere, and does not require an explanation in terms of retrieval issues. This view is further supported by the enhanced altitude differences at the evening terminator with respect to its morning counterpart, observed in both sets of VIRTIS-M data.

The inclusion of complete photochemical models in GCMs is still a work in progress for the Venus environment. Nonetheless, results by *Stolzenbach et al.* [2013] may provide insights to interpret the [CO] map of Figure 9. These authors expect a substantial increase of [CO] south of 70°S at 65 km altitude as a result of the accumulation of photochemical products at the poles by the meridional circulation. This is a similar interpretation as proposed in *Marcq et al.* [2006], *Marcq et al.* [2008], and *Tsang et al.* [2008] for values observed deeper below the clouds, at the 35 km altitude, and modeled with the LMD GCM and a passive tracer scheme in *Marcq and Lebonnois* [2013]. The decrease north of 60°S expected by the model is quantitatively consistent with our results. On the other hand, paper II demonstrated a strong decrease of VIRTIS-M data sensitivity to CO south of 70°S because of temperature inversions associated to cold collar. Consistent with this interpretation, our values here align with the a priori estimate of 40 ppm. GCM and VIRTIS-M data set are therefore consistent once intrinsic limitations of both are taken into account.

7. Conclusions

The development of a full Bayesian code for the analysis of VIRTIS-M nighttime data allowed to confirm the important role of dynamic in driving the atmospheric conditions at Venus.

1. Air temperatures between 65 and 80 km were mapped in their average values as a function of latitude (from south pole to 40°S) and local time (during night), creating a key reference for validation of Venus GCMs. These results confirm the major role of thermal tides in shaping Venus temperature fields, as already pointed out in *Tellmann et al.* [2009] and *Migliorini et al.* [2012].

2. The average temperature fields described in our previous results of paper I are confirmed qualitatively and quantitatively by the outcomes of the new algorithm presented here. Relevant differences are observed only in the lowest part of our sensitivity range (98.4 mbar, i.e., ~65 km). Here, the variable cloud top altitude available with the new code leads to lower air temperatures south of 60°S and to warmer temperatures north of 60°S. Namely, the coldest area of the cold collar at about 3LT is moved from 65°S to 70°S.

3. The new retrieval code allowed to determine average fields of cloud altitudes and [CO]. Despite the uncertainties, we confirmed an increase of cloud altitudes from the pole toward the equator also on the nightside. The higher variation observed at the evening terminator with respect to the morning terminator can be a proxy of the more vigorous meridional circulation on the dayside expected by GCMs.

4. The region of maximum [CO] above the clouds (60°S) is consistent with a relative enrichment driven by the sinking of [CO]-rich air from regions at higher altitudes associated with the mean meridional circulation, once the limitation of VIRTIS-M [CO] values in the cold collar are kept in mind.

In view of the results obtained so far, we plan to reprocess in future the entire VIRTIS-H data set with the new retrieval code, to extend these studies at all latitudes.

References

Abe, Y., A. Abe-Ouchi, N. H. Sleep, and K. J. Zahnle (2011), Habitable zone limits for dry planets, *Astrobiology*, *11*(5), 443–460, doi:10.1089/ast.2010.0545.
Driscoll, P., and D. Bercovici (2013), Divergent evolution of Earth and Venus: Influence of degassing, tectonics, and magnetic fields, *Icarus*, *226*(2), 1447–1464, doi:10.1016/j.icarus.2013.07.025.

Encrenaz, T., T. K. Greathouse, M. J. Ritcher, J. Lacy, T. Widemann, B. Bézard, T. Fouchet, C. de Witt, and S. K. Atreya (2013), HDO and SO2 thermal mapping on Venus II. The SO2 spatial distribution above and within clouds, *Astron. Astrophys.*, *559*, Article A65, doi:10.1051/0004-6361/201322264.

Gilli, G., M. A. Lòpez-Valverde, P. Drossart, G. Piccioni, S. Erard, and A. Cardesìn Moinelo (2009), Limb observations of CO_2 and CO non-LTE emissions in the Venus atmosphere by VIRTIS/Venus Express, *J. Geophys. Res.*, *114*, E00B29, doi:10.1029/2008JE003112.

Grassi, D., N. I. Ignatiev, L. V. Zasova, A. Maturilli, V. Formisano, G. A. Bianchini, and M. Giuranna (2005), Methods for the analysis of data from the Planetary Fourier Spectrometer on the Mars Express Mission, *Planet. Space Sci.*, *53*(10), 1017–1034, doi:10.1016/j.pss.2005.01.006.

Grassi, D., P. Drossart, G. Piccioni, N. I. Ignatiev, L. V. Zasova, A. Adriani, M. L. Moriconi, P. G. J. Irwin, A. Negrao, and A. Migliorini (2008), Retrieval of air temperature profiles in the Venusian Mesosphere from VIRTIS-M data: Description and validation of algorithms, *J. Geophys. Res.*, *113*, E00B09, doi:10.1029/2008JE003075.

Grassi, D., A. Migliorini, L. Montabone, S. Lebonnois, A. Cardesìn-Moinelo, G. Piccioni, P. Drossart, and L. V. Zasova (2010), Thermal structure of Venusian nighttime mesosphere as observed by VIRTIS-Venus Express, *J. Geophys. Res.*, *115*, E09007, doi:10.1029/2009JE003553.

Haus, R., D. Kappel, and G. Arnold (2013), Self-consistent retrieval of temperature profiles and cloud structure in the northern hemisphere of Venus using VIRTIS/VEX and PMV/VENERA-15 radiation measurements, *Planet. Space Sci.*, *89*, 77–101, doi:10.1016/j.pss.2013.09.020.

Ignatiev, N. I., D. V. Titov, G. Piccioni, P. Drossart, W. J. Markiewicz, V. Cottini, T. Roatsch, M. Almeida, and N. Manoel (2009), Altimetry of the Venus cloud tops from the Venus Express observations, *J. Geophys. Res.*, *114*, E00B43, doi:10.1029/2008JE003320.

Ingersoll, A. P. (1969), The runaway greenhouse: A history of water on Venus, *J. Atmos. Sci.*, *26*, 1191–1198, doi:10.1175/1520-0469(1969)026<1191:TRGAHO>2.0.CO;2.

Irwin, P. G. J., R. de Kok, A. Negrao, C. C. C. Tsang, C. F. Wilson, P. Drossart, G. Piccioni, D. Grassi, and F. W. Taylor (2008a), Spatial variability of carbon monoxide in Venus' mesosphere from Venus Express/Visible and Infrared Thermal Imaging Spectrometer measurements, *J. Geophys. Res.*, *113*, E00B01, doi:10.1029/2008JE003093.

Irwin, P. G. J., N. A. Teanby, R. de Kok, L. N. Fletcher, C. J. A. Howett, C. C. C. Tsang, C. F. Wilson, S. B. Calcutt, C. A. Nixon, and P. D. Parrish (2008b), The NEMESIS planetary atmosphere radiative transfer and retrieval tool, *J. Quant. Spectrosc. Radiat. Transfer*, *109*(6), 1136–1150, doi:10.1016/j.jqsrt.2007.11.006.

Isaacs, R. G., W.-C. Wang, R. D. Worsham, and S. Goldenberg (1987), Multiple scattering LOWTRAN and FASCODE models, *Appl. Opt.*, *26*(7), 1272–1281.

Kappel, D., G. Arnold, R. Haus, G. Piccioni, and P. Drossart (2012), Refinements in the data analysis of VIRTIS-M-IR Venus nightside spectra, *Adv. Space Res.*, *50*(2), 228–255, doi:10.1016/j.asr.2012.03.029.

Kawabata, K., D. L. Coffeen, J. E. Hansen, W. A. Lane, M. Sato, and L. D. Travis (1980), Cloud and haze properties from Pioneer Venus polarimetry, *J. Geophys. Res.*, *85*, 8129–8140, doi:10.1029/JA085iA13p08129.

Knollenberg, R. G., and D. M. Hunten (1980), The microphysics of the clouds of Venus - Results of the Pioneer Venus particle size spectrometer experiment, *J. Geophys. Res.*, *85*, 8039–8058, doi:10.1029/JA085iA13p08039.

Lebonnois, S., F. Hourdin, V. Eymet, A. Crespin, R. Fournier, and F. Forget (2010), Superrotation of Venus' atmosphere analysed with a full General Circulation Model, *J. Geophys. Res.*, *115*, E06006, doi:10.1029/2009JE003458.

Lebonnois, S., C. Covey, A. Grossman, H. Parish, G. Schubert, R. Walterscheid, P. Lauritzen, and C. Jablonowski (2012), Angular momentum budget in General Circulation Models of superrotating atmospheres: A critical diagnostic, *J. Geophys. Res.*, *117*, E12004, doi:10.1029/2012JE004223.

Marcq, E., and S. Lebonnois (2013), Simulations of the latitudinal variability of CO-like and OCS-like passive tracers below the clouds of Venus using the LMD-GCM, *J. Geophys. Res. Planets*, *118*, 1983–1990, doi:10.1002/jgre.20146.

Marcq, E., B. Bézard, Th. Encrenaz, and M. Birlan (2005), Latitudinal variations of CO and OCS in the lower atmosphere of Venus from near-infrared nightside spectro-imaging, *Icarus*, *179*(2), 375–386, doi:10.1016/j.icarus.2005.06.018.

Marcq, E., Th. Encrenaz, B. Bézard, and M. Birlan (2006), Remote sensing of Venus' lower atmosphere from ground-based IR spectroscopy: Latitudinal and vertical distribution of minor species, *Planet. Space Sci.*, *54*(13–14), 1360–1370, doi:10.1016/j.pss.2006.04.024.

Marcq, E., B. Bezard, P. Drossart, G. Piccioni, J. M. Reess, and F. Henry (2008), A latitudinal survey of CO, OCS, H_2O, and SO_2 in the lower atmosphere of Venus: Spectroscopic studies using VIRTIS-H, *J. Geophys. Res.*, *113*, E00B07, doi:10.1029/2008JE003074.

Migliorini, A., D. Grassi, L. Montabone, S. Lebonnois, P. Drossart, and G. Piccioni (2012), Investigation of air temperature on the nightside of Venus derived from VIRTIS-H on board Venus-Express, *Icarus*, *217*(2), 640–647, doi:10.1016/j.icarus.2011.07.013.

Piccioni, G., et al. (2007), The Visible and Infrared Thermal Imaging Spectrometer, *Eur. Space Agency Spec. Publ.*, *1295*, 1–27.

Rodgers, C. D. (2000), *Inverse Methods for Atmospheric Sounding: Theory and Practice*, World Scientific, Singapore.

Rothman, L. S., et al. (2009), The HITRAN 2008 molecular spectroscopic database, *J. Quant. Spectros. Radiat. Transfer*, *110*(9-10), 533–572, doi:10.1016/j.jqsrt.2009.02.013.

Schaefer, K., L. V. Zasova, D. Spaenkuch, E. A. Ustinov, and D. Oertel (1987), Structure of the middle atmosphere of Venus from analysis of Fourier spectrometer measurements aboard Venera 15, *Adv. Space Res.*, *7*(12), 17–24, doi:10.1016/0273-1177(87)90197-9.

Stolzenbach, A., F. Lefevre, S. Lebonnois, and A. Maattanen (2013), Three-dimensional modelling of Venus photochemistry, Abstract 62 presented at International Venus Workshop, Catania, Italy, 10–14 June.

Tellmann, S., M. Pätzold, B. Häusler, M. K. Bird, and G. L. Tyler (2009), Structure of the Venus neutral atmosphere as observed by the Radio Science experiment VeRa on Venus Express, *J. Geophys. Res.*, *114*, E00B36, doi:10.1029/2008JE003204.

Tice, D. S., P. G. J. Irwin, L. N. Fletcher, N. A. Teanby, J. Hurley, G. S. Orton, and G. R. Davis (2013), Uranus' cloud particle properties and latitudinal methane variation from IRTF SpeX observations, *Icarus*, *223*(2), 684–698, doi:10.1016/j.icarus.2013.01.006.

Tran, H., C. Boulet, J.-M. Hartmann, S. Stefani, M. Snels, and G. Piccioni (2011), Measurements and modeling of high pressure pure CO_2 spectra in central and wing regions from 600 to 9000 cm^{-1}, *J. Quant. Spectros. Radiat. Transfer*, *112*, 925–936, doi:10.1016/j.jqsrt.2010.11.021.

Tsang, C. C. C., P. G. J. Irwin, C. F. Wilson, F. W. Taylor, C. Lee, R. de Kok, P. Drossart, G. Piccioni, B. Bezard, and S. Calcutt (2008), Tropospheric carbon monoxide concentrations and variability on Venus from Venus Express/VIRTIS-M observations, *J. Geophys. Res.*, *113*, E00B08, doi:10.1029/2008JE003089.

Wilquet, V., R. Drummond, A. Mahieux, S. Robert, A. C. Vandaele, and J.-L. Bertaux (2012), Optical extinction due to aerosols in the upper haze of Venus: Four years of SOIR/VEX observations from 2006 to 2010, *Icarus*, *217*(2), 875–881, doi:10.1016/j.icarus.2011.11.002.

Zasova, L. V., N. Ignatiev, I. Khatuntsev, and V. Linkin (2007), Structure of the Venus atmosphere, *Planet. Space Sci.*, *55*(12), 1712–1728, doi:10.1016/j.pss.2007.01.011.